THE JOURNAL OF PHYSICAL CHEMISTRY C
A JOURNAL OF THE AMERICAN CHEMICAL SOCIETY

pubs.acs.org/JPCC

Article

Conformation-Dependent Monolayer and Bilayer Structures of an Alkylated TTF Derivative Revealed using STM and Molecular Modeling

Catarina L. Delfino,[#] Yansong Hao,[#] Cristina Martin, Andrea Minoia, Elumalai Gopi, Kunal S. Mali,* Mark Van der Auweraer, Yves Henri Geerts, Sandra Van Aert, Roberto Lazzaroni,* and Steven De Feyter*

Cite This: *J. Phys. Chem. C* 2023, 127, 23023−23033

Read Online

ACCESS | Metrics & More | Article Recommendations | Supporting Information

ABSTRACT: In this study, the multilayer self-assembled molecular network formation of an alkylated tetrathiafulvalene compound is studied at the liquid−solid interface between 1-phenyloctane and graphite. A combined theoretical/experimental approach associating force-field and quantum-chemical calculations with scanning tunneling microscopy is used to determine the two-dimensional self-assembly beyond the monolayer but also to further the understanding of the molecular adsorption conformation and its impact on the molecular packing within the assemblies at the monolayer and bilayer level.

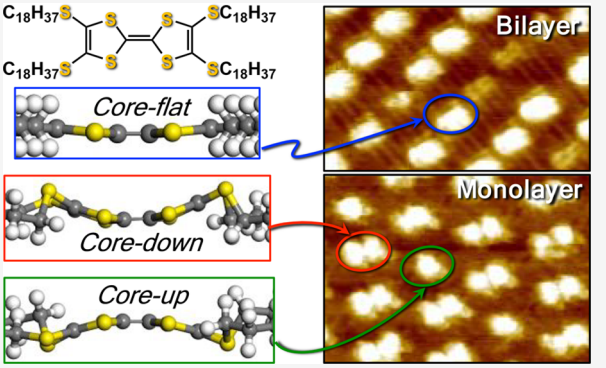

1. INTRODUCTION

Two-dimensional (2D) self-assembled molecular networks (SAMNs) of organic molecules on atomically flat, and often conductive, surfaces have been studied extensively over the past decades due to their potential applicability in different areas ranging from organic photonic or electronic devices to single-molecule switches.[1−6] In these reports, it has been demonstrated that during their formation, the surface interacts with molecules and acts as a template facilitating the formation of highly ordered supramolecular networks. Combined with other noncovalent intermolecular forces, such as hydrogen bonding,[7,8] van der Waals (vdW),[9−11] electrostatic,[12−14] dipolar,[15,16] and $\pi-\pi$ interactions,[17,18] molecular assemblies with complex architectures have been built. Therefore, building on the relationship between the structure of the SAMNs and their properties, by unraveling the role and influence of those forces on the packing, the ambition is to predict, understand and control those properties.

Among the techniques used to understand the structure of SAMNs, scanning tunneling microscopy (STM) has become a powerful tool as it allows direct observation of SAMNs on solid surfaces at (sub)molecular resolution. This high-spatial resolution brings insight into the adsorption conformations of molecules[19−21] and enables the measurement of the 2D lattice parameters, in some cases elucidating the self-assembly mechanism of the studied systems.[22,23]

Few studies have aimed to unravel the correlation between the surface confined SAMNs and the substrate induced phases (SIPs) which may be templated by the SAMNs. SIPs are polymorphic phases that form when the material crystallizes near the substrate as a thin film (∼few tens of nm in thickness). SIPs can have polymorphic structures that differ from those observed in the corresponding single crystals ("bulk" structure), and in some cases from the SAMN in contact with the substrate.[24−26] SIPs may lead to enhanced charge transport mobility in the field of organic semiconductors[27,28] and solubility in pharmaceutics.[29,30]

SAMNs and SIPs are conceptually related as a SAMN can be seen as the thinnest SIP with only one-molecular layer thickness. Efforts have been made to investigate molecular self-assembly beyond monolayers,[31,32] but there are still some challenges. One of the bottlenecks for the characterization of thin SIPs with techniques such as X-ray diffraction is the low signal-to-noise ratio posing constraints on the detection limit.[33−35] On conductive substrates, techniques like STM may provide valuable input and allow the characterization of

Received: July 21, 2023
Revised: October 22, 2023
Accepted: October 23, 2023
Published: November 15, 2023

up until few-layer-thin structures with submolecular resolution.[31] However, relying only on STM for the structural characterization of thin films on conductive substrates has its limitations as well, and often complementary atomistic simulations[36,37] are required to achieve deep understanding. A good starting point is the study of the molecular conformation and structural organization of multilayer SAMNs, which acts as bridging stage between monolayer SAMNs and SIPs.

Bearing this in mind, in this study we use a combined experimental and theoretical approach, where the self-assembly of an alkylated tetrathiafulvalene (TTF) derivative, i.e., tetrakis(octadecylthio) tetrathiafulvalene (**1**, Figure 1), is

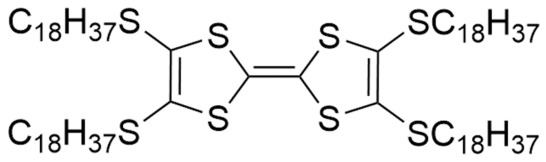

Figure 1. Molecular structure of tetrakis(octadecylthio)-tetrathiafulvalene, **1**.

investigated at the solution/graphite interface. The choice of this molecule is based on its versatile properties, which allows it to be used for a wide range of applications,[38−41] as well as its compatibility with STM[42] as thin-film characterization tool. Studying the self-assembly behavior of **1** *in situ* with STM together with DFT and force field calculations not only allows the visualization of the 2D assembly beyond the monolayer level, but also brings insight into the importance of molecular conformation on the multilayer packing.

2. METHODS

2.1. Synthesis of 1. 4,4′,5,5′-Tetrakis(octadecylthio)-2,2′-bi(1,3-dithiolylidene) or **1** was synthesized in two steps from commercially available [1,3]dithiolo[4,5-*d*][1,3]dithiole-2,5-dione. Initially, [1,3]dithiolo[4,5-*d*][1,3]dithiole-2,5-dione was treated with NaOMe in methanol (0.5 M, 9.6 mL, 2 equiv) to generate disodium dithiolate which was trapped by octadecyl bromide in the presence of DMF as a solvent at 65 °C. The obtained dialkylated compounds underwent dimerization in the presence of triethyl phosphite (10 equiv. excess) at 120 °C for overnight, resulted in formation of the dimeric product **1**, which was purified by repeated washing with cold methanol (>99% purity by NMR) (see section 1 in the Supporting Information).

2.2. Preparation of Self-Assembled Layers and STM Characterization. A stock solution of **1**, ($C = 7.5 \times 10^{-4}$ M) was prepared by dispersing 1 mg of the compound per 1 mL of 1-phenyloctane (1-PO) followed by sonication for 1 h. 1-PO was obtained from Sigma-Aldrich (>99%) and used without further purification. The stock solution was diluted further with 1-PO to prepare a concentration series. One should note that the actual solubility of **1** at room temperature is only in the order of 3.7×10^{-5} to 4.2×10^{-5} M (*vide infra*). All solutions, where the formal concentration of **1** exceeds this limit, are dispersions. All solutions were sonicated for 5 min before use. This procedure homogenized and stabilized the dispersions, possibly by decreasing the size of particles of dispersed solid **1**. All STM experiments were performed at room temperature (21−23 °C), using a PicoLE (Agilent) machine operating in constant-current mode with the tip immersed in the liquid. STM tips were prepared by mechanically cutting a Pt/Ir wire (80%/20%, diameter 0.2 mm). Prior to imaging, a drop of solution was placed onto a freshly cleaved surface of HOPG. The images were corrected for drift via scanning probe image processor (SPIP) software, using the recorded graphite images for calibration purposes, allowing accurate unit cell determination. The unit cell parameters were determined by examining several images. The imaging parameters, tunneling current (I_{set}), and sample bias (V_{bias}), are indicated in each figure caption.

2.3. UV−Vis Spectroscopy Characterization. The UV−vis absorption spectra were recorded using a Lambda 950 spectrophotometer with blocked beam and blank corrections. To record UV−vis spectra as a function of the temperature, a temperature controller was used and every time that the required temperature was stabilized, a UV−visible spectrum was recorded.

2.4. DFT Geometry Optimizations and STM Simulations. All DFT calculations were performed using the 4.1 version of the SIESTA package.[43] The exchange-correlation functional was described by the PBE functional[44] within the general gradient approximation. The valence electrons were described by a numerical double-ζ polarized (DZP) basis set with a reasonable mesh-cutoff of 250 Ry, while the core electrons were treated by the Troullier−Martins pseudopotentials.[45] The Brillouin zone was sampled using a Monkhorst−Pack grid[46] of $(1 \times 1 \times 1)$. A single point is sufficient for sampling as the dimension of the smallest unit cell employed in the calculations is already relatively large: around 25 and 30 Å in X and Y direction, respectively. Along the Z direction, a distance of 60 Å was used to avoid the artificial interactions due to periodic boundary conditions. van der Waals interactions were incorporated in the calculations through the Grimme corrections.[47] For geometry optimizations, the atomic positions of the adsorbed molecules were relaxed until the interatomic forces are smaller than 0.04 eV/Å. All simulated STM images were generated based on the force-field-optimized geometries. In this study, the geometry optimizations and STM image simulations were carried out on adsorption systems that involve TTF molecules having alkyl chains with different lengths. In SIESTA, the integration of the local density of states (LDOS) was calculated over an energy window that is determined by the experimental bias voltage used for recording the STM images. The simulated STM images were then generated from this integrated LDOS, based on the Tersoff−Hamann approximation using the WSxM software.[48]

2.5. Molecular Mechanics (MM) and Dynamics (MD) Simulations. All force-field calculations were carried out in the Forcite module as implemented in the BIOVIA Materials Studio 2018.[49] The Universal Force Field[50,51] was employed in all MM and MD simulations described in this paper, which has been validated by previous studies.[52] ESP charges calculated at the DFT level with the Gaussian 16 simulation package[53] and Gasteiger charges were combined and used as the atomic charges in the force-field calculations. For the calculation of ESP charges, the B3LYP[54−58] functional was employed with the 6-31+G(d,p) basis set. MD simulations for the assemblies of TTFs were performed in the *NVT* ensemble (constant number of particles, volume, and temperature) with the Nosé−Hoover−Langevin (NHL)[59] thermostat. The HOPG substrate was represented by a single graphene layer whose atoms are frozen during the simulations, since the physisorption of TTFs

https://doi.org/10.1021/acs.jpcc.3c04913
J. Phys. Chem. C 2023, 127, 23023−23033

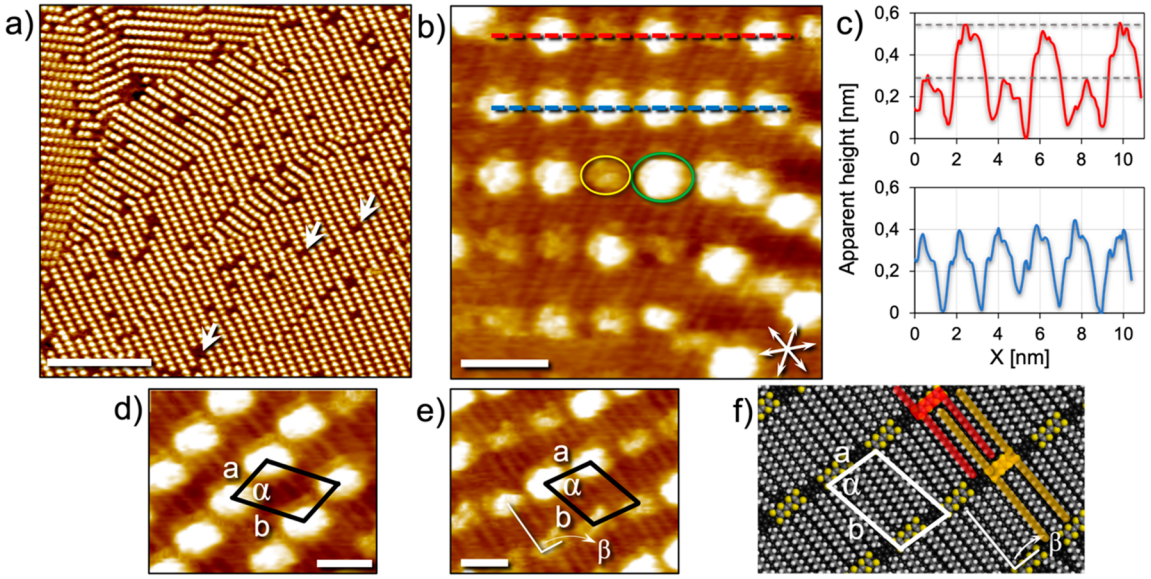

Figure 2. Self-assembly of **1** ($C = 7.5 \times 10^{-4}$ M) at the 1PO/graphite interface. (a) Large scale STM image (scale bar = 20 nm) showing the overall morphology of the physisorbed SAMN formed by **1**. The white arrows highlight the defects in the SAMN. (b) Smaller scale STM image (scale bar = 3 nm) showing variable STM contrast within the SAMN which we ascribe to the formation of a bilayer. (c) Profiles corresponding to the red and blue dashed lines in panel b highlighting the differences in the apparent heights of molecules in the upper and lower layers. (d, e) Small scale images showing the unit cells within the upper (d) and lower (e) layers. Imaging parameters (a, b, d, e): I_{set} = 70 pA to 90 pA, V_{bias} = −0.750 V to −1.000 V. (f) A molecular model depicting the packing arrangement of **1** in the first layer adsorbed on the graphite surface. Two molecules, one in red, and one in orange, highlight the interdigitation of the alkyl chains.

on HOPG is not expected to change the geometry of the substrate underneath. The quench-MD approach (Figure S1 in Supporting Information), where the structures are optimized periodically during the MD run, was used to refine the initially optimized structures, thus enabling a better convergence toward the most stable structure.

3. RESULTS AND DISCUSSION

3.1. Self-Assembly of 1 at the 1-Phenyloctane/HOPG Interface: STM. SAMNs of **1** were obtained by drop casting a 1-PO solution onto freshly cleaved HOPG and the STM imaging was carried out at the 1-PO/HOPG interface. **1** promptly forms a highly ordered SAMN upon physisorption at the 1-phenyloctane/HOPG interface. Figure 2a shows a typical large scale STM image of the SAMN where it is possible to distinguish the bright TTF moieties from the alkyl substituents, which are adsorbed in the darker regions. The higher tunneling current recorded over the TTF moieties is in line with their electron-rich nature, whereas the darker areas corresponding to lower tunneling current indicate the regions where the alkyl chains are adsorbed. The rows of bright features and dark regions alternate. The STM images show defects (white arrows, Figure 2a) which we ascribe to missing TTF molecules.

Smaller scale STM images such as the one presented in Figure 2b highlight a peculiar feature of the SAMNs of **1** formed at the 1-PO/HOPG interface. The bright features within the SAMN appear with different levels of contrast. Two different levels can be identified within the STM image provided in Figure 2b wherein the brighter features (green oval) also appear slightly larger than the dimmer features (yellow oval). Based on the variable contrast within the SAMN, we conclude that **1** forms a bilayer at the 1-PO/graphite interface under these experimental conditions with the bright features corresponding the molecules adsorbed in the second layer whereas the darker moieties are the molecules adsorbed directly on the HOPG surface. Besides the difference in the STM contrast, the formation of the bilayer can also be inferred from the difference in the measured apparent height of the TTF cores as depicted in the line profiles presented in Figure 2c. We conclude that the defects observed in large scale images (white arrows, Figure 2a) are thus missing molecules in the second layer and the smaller scale images allow the observation of the layer beneath the top layer.

Parts d and e of Figures 2 show STM images highlighting the unit cells of the top and the (partially visible) bottom layers, respectively. The unit cells are comparable (Table 1).

Table 1. Unit Cell Parameters for the SAMNs of 1

	Unit cell (exp)			
	a (nm)	b (nm)	α (deg)	Packing density (molecules/nm^2)
Bilayer	1.8 ± 0.1	2.9 ± 0.2	69.0 ± 4.0	0.209
Bottom layer (*sim*)	1.8	2.9	71.7	0.202
Monolayer (*exp*)	2.2 ± 0.2	3.8 ± 0.2	74.0 ± 4.0	0.122
Monolayer (*sim*)	2.1	3.7	73.4	0.134

The striped features running in between the rows of TTF cores are ascribed to the alkyl chains. Based on the average distance between the adjacent rows of TTF cores (2.6 ± 0.2 nm), we conclude that the octadecyl chains are fully extended and adsorbed on the HOPG surface. All four chains per molecule are adsorbed on the surface which are always oriented along one of the main symmetry axes of the graphite lattice and make an angle of $\beta = 102 \pm 5°$ with respect to the row of TTF cores (Figure 2e). We hypothesize that the bilayer SAMN is governed by $\pi-\pi$ stacking between TTF cores and is stabilized

https://doi.org/10.1021/acs.jpcc.3c04913
J. Phys. Chem. C 2023, 127, 23023−23033

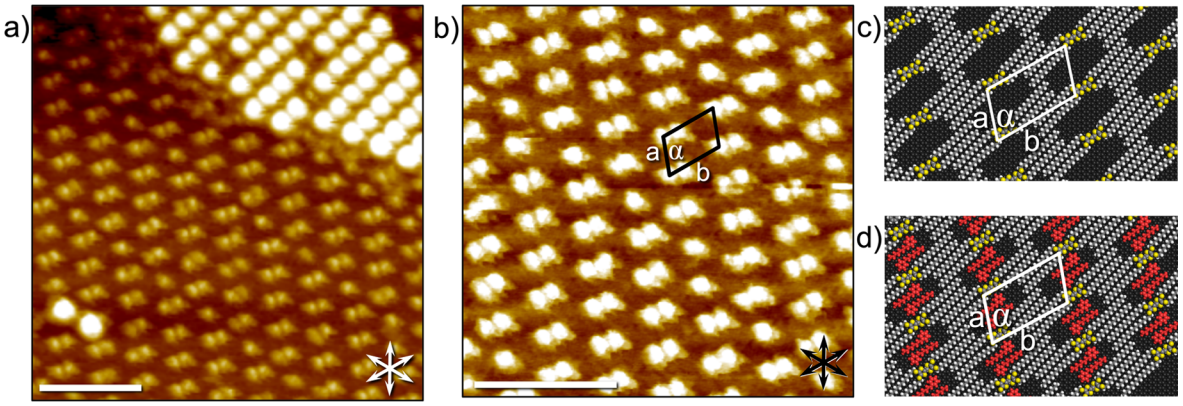

Figure 3. Self-assembly of **1** at the 1-PO/graphite interface a few hours after deposition of the solution. (a) STM image showing the coexistence of the monolayer and the bilayer structures (scale bar = 10 nm). (b) STM image of the monolayer structure with overlaid unit cell (scale bar = 10 nm). Graphite symmetry axes are presented in the lower left corner of the STM images. Imaging parameters (a, b): I_{set} = 70pA to 90 pA, V_{bias}= −0.750 V to −1.000 V. (c) A force field-optimized structural model for the molecular arrangement of the monolayer considering the experimentally measured unit cell. (d) The same model as in part c but considering the coadsorption of the solvent molecules (red).

by the interdigitation of the alkyl chains between the first layer at the surface. A molecular model of the first layer in contact with the surface was built using these considerations and then further refined using MM/MD simulations (*vide infra*) and is presented in Figure 2f. The model depicts close-packed assembly of **1** where pairs of alkyl chains on either side of the TTF core are interdigitated with those of molecules in the neighboring rows. The lattice parameters obtained from simulations are in close agreement with those obtained experimentally (Table 1).

In addition to the bilayer assembly, which is the dominant pattern observed under these experimental conditions, another molecular packing was also observed. This new structure was observed a few hours after deposition of the solution of **1**. Figure 3a shows the STM image of the second network coexisting with the previously described bilayer structure. In contrast to the bilayer, here the network structure is dominated by double lobed bright features. Single lobed features are also observed albeit to a lesser extent (29%). Much like in the bilayer assembly, the molecules organize in rows. In areas with exclusive double-lobed features, the average double-lobe to double-lobe distance is 2.2 ± 0.2 nm. The average orthogonal intermolecular distance between adjacent rows is 3.4 ± 0.1 nm. A characteristic unit cell for the assembly is represented in Figure 3b which exhibits lattice parameters distinctly larger than those for the bilayer (Table 1) making this a rather loosely packed assembly. The darker regions do not exhibit any specific contrast which could be unambiguously ascribed to the alkyl chains. The absence of point defects and the fact that scanning at high currents (scanning at shorter tip sample distances) revealed graphite lattice indicates that the new structure can be ascribed to a monolayer.

Assuming that the bright features correspond to the TTF core of **1**, a molecular model was built which is presented in Figure 3c. The model depicts a rather open structure where the molecules are arranged in rows with the alkyl chains fully extended and arranged in pairs instead of interdigitation. This leaves quite some open areas in between the molecules which are mostly occupied by solvent molecules, providing additional stability to the network. A molecular model presented in Figure 3d shows this possibility where pairs of 1-PO molecules are coadsorbed between the molecules of **1**. We hypothesize that such packing is stabilized by interactions between aromatic−CH group on the phenyl ring of 1-PO and the sulfur atoms on the core of the neighboring molecule of **1** (see Figure S2 in the Supporting Information). Invoking such stabilization is not unreasonable as existence of hydrogen-bond-like interactions between −CH donors and sulfur acceptors has been reported earlier.[60] Furthermore, the coadsorption of the solvent molecules does not distort the unit cell of the network which remains the same after coadsorption of 1-PO. To understand the origin of the contrast difference in the features observed in the STM images for the two structures and to shed light on the composition of the new structure, we resorted to MM/MD simulations.

3.2. Adsorption Conformation of Single Molecule and STM Contrast: MM/MD and STM Simulations. The striking contrast difference between the features observed in the bilayer (oval or rectangular) and the monolayer (single and double lobed) structures can be traced back to the conformation of TTF cores. Previous theoretical studies on TTF derivatives have revealed that for the simplest alkylated TTF, (tetrakis(methylthio)tetrathiafulvalene (TTF-$(SC_1)4$), the TTF core is boat-shaped,[61−63] which is also confirmed by our DFT calculations (Figure S3 in the Supporting Information). We hypothesize that the nonplanar geometry of the TTF core and in turn its adsorption geometry on the graphite surface is a key aspect toward understanding the experimentally observed STM contrast. To understand the factors contributing to the peculiar STM contrast of the features observed in the monolayer and to determine the adsorption conformation of **1** within the experimentally observed assembly, elaborate DFT and force-field simulations were performed. Harmonic restraints were applied on **1** in all the force-field calculations to reproduce the boat-shaped conformation of the TTF core. To have a better consistency with the molecular geometry optimized at DFT-level, extra harmonic restraints were applied to the torsion angle φ and its three equivalents (Figure S4 in the Supporting Information) in all force-field calculations. The equilibrium angle for these restraints is set at 160 deg. In this way, an energy penalty is applied when the molecule geometry deviates from the boat-like shape as revealed by the DFT optimizations. Force constants of such restraints are determined to be 25 kcal/(mol/deg), at which the DFT-optimized adsorption conformation of TTF-$(SC_1)_4$ on HOPG is successfully reproduced

https://doi.org/10.1021/acs.jpcc.3c04913
J. Phys. Chem. C 2023, 127, 23023−23033

by the force field simulations (Figure S4b in the Supporting Information).

In previously reported STM data on TTF derivatives,[52] TTF cores were imaged as featureless rectangular bright features similar to the STM images recorded in this study for the bilayer. In this previous study, the STM contrast was attributed to a planar TTF core adsorbed on the surface, held together by interdigitated alkyl chains. However, this hypothesis was not examined thoroughly using atomistic simulations. Figure 4a shows the adsorption conformation of **1** on the graphite surface with the TTF core initially in a boat-like conformation resembling that calculated for TTF−$(SC_1)_4$. Upon minimization, the TTF core of **1** clearly goes through planarization (Figure 4a,b) in the same way as proposed in earlier report.[52] This planarization, which is also found in the DFT calculations (see Figure S4 in the Supporting Information), is probably due to increased $\pi-\pi$ interactions between the TTF core and the graphite surface. Given its planar geometry, we will refer to this conformation as the *core-flat* conformation in the following text. To understand the STM contrast of the *core-flat* conformation, STM simulations were carried out on this adsorption geometry. A simulated STM image is also depicted in Figure 4b together with the corresponding STM image. The TTF core appears as a rectangle with uniform brightness in the simulated STM image, closely matching the contrast in the experimental STM image of the bilayer assembly.

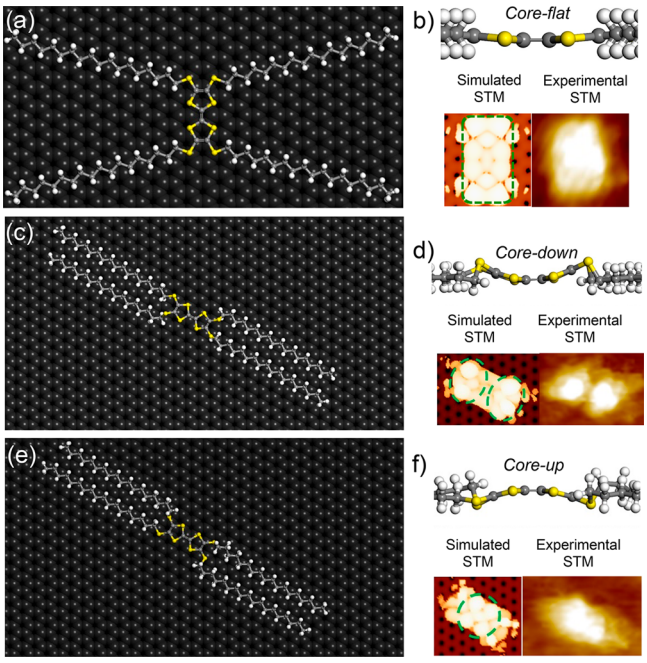

Figure 4. Force-field-optimized molecular models for the adsorption of **1** in *core-flat* (a, b), *core-down* (c, d) and *core-up* (e, f) conformation. Panels b, d, and f show zoomed-in side-view of the TTF core for each conformation and the simulated STM image at the experimental bias voltage, V_{bias} = −1.000 V, respectively. The experimental STM images are also shown at the right side of each simulated image for the sake of comparison. The green dashed shapes correspond to the brightest areas in the simulated STM images.

If the core planarization does not occur, the inherent boat-like shape of the TTF core allows for two additional adsorption geometries for **1**, which are not equivalent, namely *core-down* (Figure 4c,d, "the boat is afloat") and *core-up* (Figure 4e,f, "the boat has capsized"). For these two conformations, the octadecyl chains are tentatively paired into two groups. The arguments in favor of this arrangement are (1) the lack of any experimental evidence for the interdigitation of alkyl chains in the monolayer, in contrast to what observed in the bilayer assembly, and (2) the fact that the unit cell of the monolayer assembly is larger than that of the bilayer assembly. Considering these possibilities, alkyl chain pairing is presumed as a reasonable packing arrangement for the alkyl chains adsorbed on the substrate.

Force-field-optimized structures for *core-down* (Figure 4c) and *core-up* (Figure 4d) adsorption geometries show that, after optimization, (i) the alkyl chains remain paired and (ii) the boat-like TTF core is preserved in both conformations (Figure 4d,f). STM simulations were also performed on these geometries and are presented in (Figure 4d,f). For the *core-down* geometry, the simulated STM image shows an overall rectangular shape with brighter regions at both ends of the TTF core (Figure 4d, green dashed ovals) and a less bright region at the center of the molecule. We attribute the two brighter regions to the protruding sulfur atoms of the bent TTF core. The appearance of this simulated image is consistent with the double-lobed features in the monolayer assembly. On the contrary, the simulated STM image for the *core-up* conformation shows higher brightness at the center of the molecule (Figure 4d, green circle). This is directly related to the *core-up* adsorption geometry where the central part of the TTF core stays at a higher elevation with respect to the surface of graphite. This simulated image corresponds to the single-lobed features in the experimentally observed STM image of the monolayer of **1**. It is therefore likely that the single- and double-lobed features observed in the monolayer of **1** correspond to TTF molecules with dissimilar adsorption geometries, namely *core-up* and *core-down*, respectively. Furthermore, both *core-up* and *core-down* conformations show excellent ability to self-assemble at the monolayer level. Thus, a monolayer consisting of molecules with *core-up* and *core-down* is feasible. This was verified by constructing a molecular model of the monolayer made up of *core-down* geometries and inserting a few molecules with *core-up* geometry. Both overall packing and the lattice parameters were found to be well-preserved after optimization, which indicates that mixing between the two geometries occurs without causing any significant distortion to the original lattice and hence supports the experimental observation of the monolayer with mixed adsorption geometries (Figure S5 in the Supporting Information).

Another peculiar aspect of the experimentally observed monolayer is that the surface coverage of the double-lobed species is significantly higher than its single-lobed counterpart. To understand the discrepancy in the surface coverage of the *core-up* and *core-down* adsorption geometries, we estimated their potential energy and correlated it to their relative stabilities. In the optimized structures, the potential energy for *core-down* geometry is −141.8 kcal/mol while it is only −125.3 kcal/mol for the *core-up* geometry. Thus, the *core-down* geometry of **1** (Figure 4c,d) is the preferred adsorption geometry in the monolayer, which explains the higher surface coverage of double-lobed features in the experimentally observed monolayer. The *core-flat* conformation in Figure 4a,b shows an intermediate stability with a potential energy of −136.0 kcal/mol. We believe that the superior stability of the *core-down* geometry is due to the stronger interaction between

https://doi.org/10.1021/acs.jpcc.3c04913
J. Phys. Chem. C 2023, 127, 23023−23033

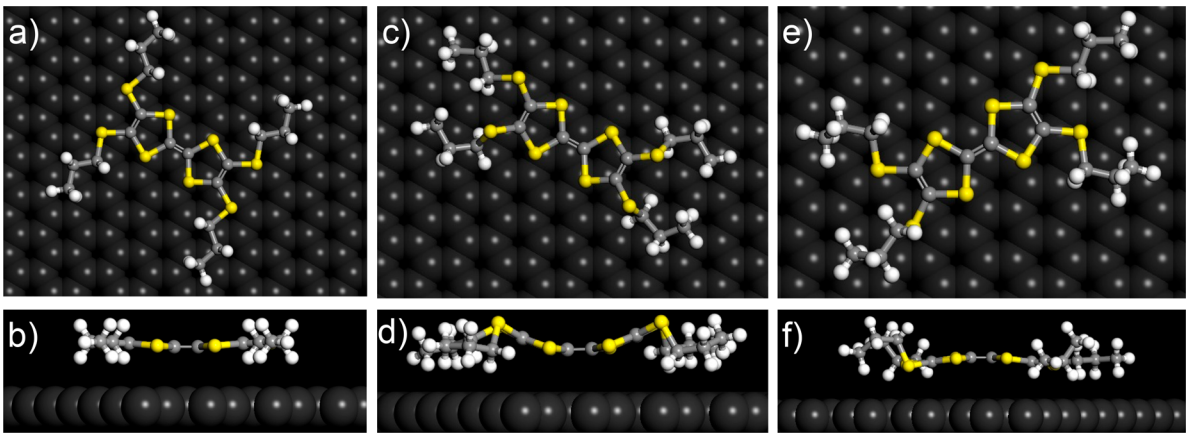

Figure 5. Force-field optimized atomistic model of TTF-$(SC_3)_4$ in (a, b) *core-flat*, (c, d) *core-down*, and (e, f) *core-up* conformation.

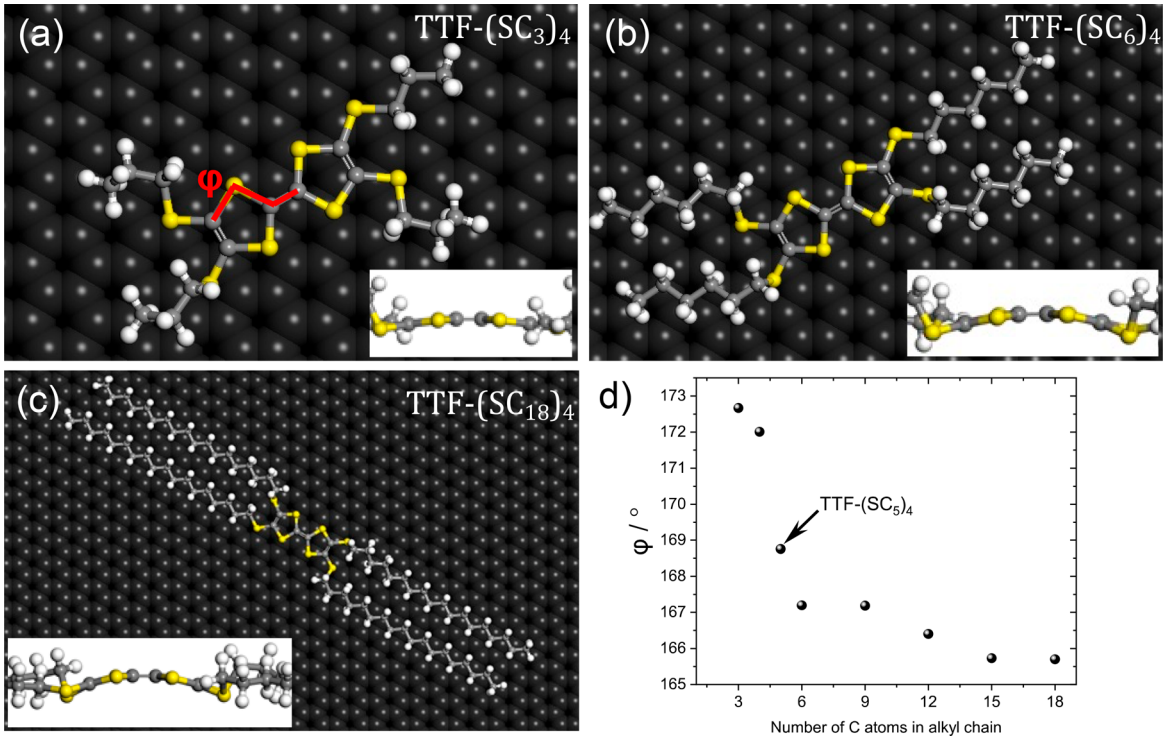

Figure 6. Force-field optimized adsorption geometries of (a) TTF-$(SC_3)_4$, (b) TTF-$(SC_6)_4$, and (c) TTF-$(SC_{18})_4$ in *core-up* conformation. The insets are side views of the TTF core to better visualize the molecular planarization. The torsion angle φ associated with molecular planarization is labeled in part a. There are four equivalent torsion angles in the TTF core. Only one is shown here for the sake of clarity. (d) A plot showing the changes in the torsion angle φ as a function of chain length.

the paired alkyl chains. On the contrary, the *core-up* geometry (Figure 4e,f) shows the poorest stability, despite similar pairing of alkyl chains. This could be explained by its weaker interactions with the substrate owing to the adsorption geometry of the core. For the *core-up* geometry, in fact, the TTF core of the molecule does not adsorb in the most favorable way on the substrate (Figure S6 in the Supporting Information). Based on the experimental STM data, STM simulations and energetic calculations, we can conclude that the three types of contrast we see in the experimental STM images can be attributed to three different absorption geometries of **1** within the assembly. The rectangular, double-lobed, and single-lobed features are successfully correlated with *core-flat, core-down,* and *core-up* conformations, respectively.

It is worth noting here that, as demonstrated by the experimental data and the STM simulations, the arrangement of the alkyl chains plays a crucial role in determining the adsorption conformation of alkylated-TTFs on the surface. The *core-flat* conformation is only stable when the alkyl chains are perpendicular to the long axis of the TTF core, while the *core-down* and *core-up* conformations are obtained only when the alkyl chains of molecules are paired and are oriented along the long axis of the TTF core. To demonstrate that this is the case, we performed a systematic study on how the length of the alkyl chains affects the geometry of the TTF core once the molecules adsorb on graphite. Figure 5 shows the optimized geometries for TTF−$(SC_3)_4$ adsorbed on the HOPG surface in *core-flat* (Figure 5a,b), *core-down* (Figure 5c, d) and *core-up* (Figure 5e,f) conformation. Their input structures have the

https://doi.org/10.1021/acs.jpcc.3c04913
J. Phys. Chem. C 2023, 127, 23023−23033

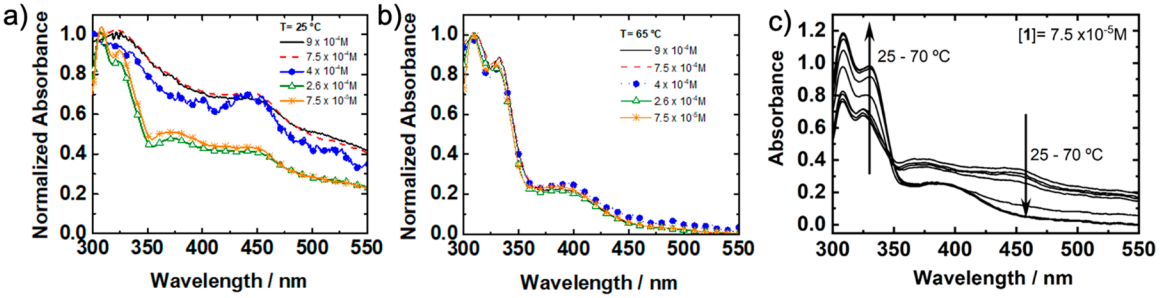

Figure 7. UV−vis absorption spectra of **1** in 1-PO (normalized at the maximum) as a function of concentration recorded at (a) 25 °C and (b) 65 °C. (c) Temperature dependence of the UV−vis absorption spectra of **1** in 1-PO for 7.5×10^{-5} M.

same geometry as that for **1** adsorbed on the graphite surface, except for the shorter length of the alkyl chains.

In contrast to that in the case of **1**, after optimization, it is the *core-flat* conformation that shows the best stability instead of the *core-down* conformation. The potential energy of the *core-down* and *core-up* conformation is 24.3 and 27.4 kcal/mol higher, respectively. Using the same input structures, identical stability ranking, and geometries were obtained from optimizations at the DFT level, which confirms the appropriate description of the adsorption geometry by the force-field. The propyl side chains are roughly paired in the *core-down* and *core-up* conformations of TTF−$(SC_3)_4$ although a much weaker interaction is expected, due to the shortened length. For this reason, a lower stability is gained from the alkyl chains for TTF−$(SC_3)_4$, making the relative energetic stability reversed between the *core-flat* and *core-down* conformation, compared to **1**. The *core-up* conformation still suffers from the less favored geometry and is again the least stable structure.

A 100 ps-long MD simulation at 298 K was then performed on the three optimized structures of TTF−$(SC_3)_4$. At the end of these simulations, both *core-down* and *core-up* geometries converted into the *core-flat* geometry (Figure S7 in the Supporting Information), which is not the case for molecule **1**. This structural conversion and the change in the relative energetic stabilities indicates that the core conformation of the adsorbed alkylated-TTFs is very sensitive to the arrangement of the alkyl chains. When adsorbed on the substrate, the presence of long and paired alkyl chains preserves the original boat-like conformation existing in the isolated molecule. The long and paired alkyl chains interact strongly between themselves and with the substrate. They therefore act as anchors, hindering the planarization of the molecule. This is not the case for the *core-flat* conformation, where the planarization of the molecule is easier since the hindrance from paired alkyl chains is absent.

Finally, the effect of the alkyl chains on the planarization of the molecule was further investigated by modeling the adsorption of alkylated TTFs having chains with different lengths in the same *core-up* conformation. The optimized geometries of TTF-$(SC_3)_4$, TTF-$(SC_6)_4$ and TTF-$(SC_{18})_4$ (=compound **1**) are shown in Figure 6. The torsion angle (φ, Figure 6a) associated with the planarization of the molecule was measured. With this exercise, the effects of the alkyl side chains on the conformation of the core can be discerned in a more quantitative way. The average values of this torsion angle increase gradually from 165.5° for TTF-$(SC_{18})_4$ to 172.3° TTF-$(SC_3)_4$, which corresponds to the most planarized conformation (φ closest to 180°). Increase of torsion angle φ (more planarization) as a function of decreasing alkyl chain length is observed for a broad coverage of alkylated TTFs (Figure 6d). The planarization is suppressed for TTFs with longer alkyl chains because the pairing of those chains and the subsequent van der Waals interactions between them prevails over the interactions between the TTF core and the graphite surface.

While the discussion provided above rationalizes the structure and constitution of the experimentally observed self-assembled monolayer and the bilayer, it does not necessarily explain the driving force for the formation of the two structures. To shed light on this aspect, we undertook a systematic concentration dependent STM study. Considering the difference in the packing density of the bilayer and the monolayer, increasing the concentration of **1** should favor the bilayer structure for concentrations below the solubility limit of **1**, which was estimated to be situated in the range of 3.7 to 4.2 $\times 10^{-5}$ M (*vide infra*). When the amount of **1** added to 1-PO exceeds the solubility limit, solid **1** is present besides dissolved **1** at a concentration equal to the solubility limit and a potential equilibrium between the monolayer and bilayer structure is no longer expected to shift upon adding more **1** to the 1-PO solution. Contrary to our expectation though, upon decreasing the formal concentration of **1** by diluting the solution, the bilayer network remains the dominant structure. In fact, for the lowest concentrations used, only a fraction of the HOPG surface was found to be covered by the bilayer of adsorbed **1** (Figure S8 in the Supporting Information). This unexpected behavior can be attributed to a packing of the adsorbed **1** that is determined by kinetic rather than thermodynamic control or to the formation of aggregates of **1** in solution.[64] To further understand the behavior of **1** in solution we carried out UV−vis spectroscopy measurements in 1-PO.

3.3. Behavior of 1 Dissolved in Solution: UV−Vis Spectroscopy. We probed the concentration (7.5×10^{-5} M to 9.0×10^{-4} M) and temperature (25 to 65 °C) dependence of the UV−vis spectra of **1** in 1-PO. Figure 7a shows an apparent concentration dependence of the normalized UV−vis spectra of **1**, which even at the lowest concentration differ from those of dilute solutions of alkyl- or thioalkyl-substituted TTF derivatives in several solvents.[65−69] However, the normalized spectra recorded for the same concentration range at 65 °C are identical over the concentration range used (Figure 7b). Their features, consisting of a maximum at 307 nm, a shoulder at 329 and 380 nm, and a long wavelength tail extending to 500 nm, match those of tetrathioalkyl substituted TTF derivatives in dilute solution, as well as calculated spectra of tetramethylbis-(ethylenedithio)tetrathiafulvalene.[67−69] Long wavelength tails, extending sometimes to 1400 nm, were reported for thin layer TTF derivatives.[70−74] For UV−vis spectra obtained at higher

https://doi.org/10.1021/acs.jpcc.3c04913
J. Phys. Chem. C 2023, 127, 23023−23033

temperatures (Figure 7b), the short wavelength maximum and shoulder become more prominent, while at longer wavelengths the transmittance (above 350 nm) is increased systematically, and the weak bands at 374 and 446 nm disappear in favor of the 380 nm species. The maximum at 307 nm and the shoulder at 329 nm are characteristic for monomers as upon aggregation these transitions shift to 297 and 317 nm, respectively.[68] From the absorbance at the maximum at 307 nm and the shoulder at 380 nm, molar extinction coefficients of respectively 1.6×10^4 $M^{-1}cm^{-1}$ and 3.6×10^3 $M^{-1}cm^{-1}$ can be obtained, which are close to the molar extinction coefficients found for TTF or alkyl substituted TTFs.[65,66] Also in the long wavelength tail the absorbance is compatible with molar extinction coefficients reported for TTF.[65] Therefore, the spectra obtained at 65 °C allow us to conclude that up to a formal concentration of 9.0×10^{-4} M a solution of **1** in 1-PO only contains monomers of **1** at 65 °C.

At lower temperatures (Figure 7a,c), the transmittance systematically increases below 350 nm while above 350 nm the opposite occurs. Furthermore, the shoulder around 380 nm splits into a weak band around 374 and 446 nm while a long wavelength tail extending beyond 550 nm develops. The increase of the absorption at 400 nm is too large to be attributed to the low oscillator strength of $1^1A_1 \rightarrow 2^1A_1$ transition or to transitions to a triplet state.[63,69,75] At first sight, the absorbance close to 450 nm could be ascribed to molecular aggregates. However, the outsized shift for J-type or H-type aggregates (from 380 to 446 nm or 3590 cm^{-1}),[76−79] together with the absence of a blue shift of the 307 nm band and the 329 nm shoulder at 25 °C[69] when comparing spectra at 65 and 25 °C, make it highly unlikely that an equilibrium between monomers and small aggregates explains the temperature and concentration dependence of the spectra. Another plausible explanation is the formation of the $TTF^{\circ+}$ radical cation since TTF and its derivatives are easily oxidized. The absorption bands of the radical cation of TTF and thio-alkyl substituted TTFs are situated at 430 nm, 495 nm, 580 nm and between 750 and 850 nm, respectively, which could explain the increased absorption at wavelengths longer than 400 nm.[73,74,80−83] However, the reversible nature of the temperature dependence would indicate that the $TTF^{\circ+}$ radical cation is reduced back to TTF which is improbable in the absence of a reducing agent.

As there is no plausible explanation for an increased absorbance above 400 nm at room temperature compared to 65 °C, the observed loss of transmittance above 400 nm at room temperature is most likely related to light scattering by particles of undissolved TTF, as was previously observed for a vapor deposited film of dimethyl-TTF.[71] Since at 25 °C part of the added **1** is present in the solid state, the actual concentration of dissolved **1** is lower than the formal concentration of 7.5×10^{-5} M. This explains why the absorbance at 307 and 329 nm has been reduced from respectively 1.20 and 1.00 at 70 °C to 0.61 and 0.48 at 25 °C. The values for the absorbance at 25 °C are corrected for light scattering because at 500 nm there is no absorption at 65 °C, and hence the apparent absorption at 500 nm at 25 °C (0.21) is attributed to light scattering. When we make the conservative estimate that the light scattering at 307 and 329 nm is identical with that at 500 nm, the apparent absorbance at 307 and 329 nm, which amounts to respectively 0.82 and 0.69, has to be reduced to 0.61 and 0.48. Hence at 25 °C the concentration of dissolved **1** is reduced from 7.5×10^{-5} M to $3.7 \pm 0.1 \times 10^{-5}$ M. As our correction for light scattering at 25 °C is probably a conservative one, the actual absorbance at 307 and 329 nm and the corresponding solubility limit should be considered as an upper limit. The UV−vis spectra of **1** recorded as a function of concentration and temperature allow to conclude that (1) At 25 °C, the solubility limit of **1** is somewhere between 3.7×10^{-5} M to 4.2×10^{-5} M. (2) At 25 °C, the solutions of **1** with a formal concentration of 7.5×10^{-5} M or higher are a heterogeneous mixture of a saturated solution of **1** and solid **1**, possibly present in the form of microcrystals. (3) In 1-PO, there is no evidence for aggregation of **1** to dimers or trimers between 25 and 70 °C (also see Figure S9 in the Supporting Information).

Even though the UV−vis absorption spectroscopy does not show strong evidence for preaggregation of **1** in 1-PO solution, it is clear is that there is a fraction of undissolved material at room temperature for a formal concentration of **1** of 4×10^{-5} M and higher. This could affect the free monomer concentration at the liquid−solid interface. Also, micro- or nanoparticles of **1** present in solution may dissociate upon coming in contact with the substrate, as previously reported.[84] Furthermore, kinetic effects may play a role in affecting the on-surface monolayer to bilayer ratio; the monolayer being the kinetically controlled structure and the bilayer the thermodynamically one.

While the formation of bilayer is not expected in the low concentration regime, one can rationalize such behavior by considering the binding energies of molecules adsorbed in the monolayer and those adsorbed in the second layer of the bilayer. Such binding energy estimates the energy gained by the molecules when incorporated in a self-assembly with respect to an isolated molecule adsorbed on the substrate. The binding energy was calculated as

$$E_{bind} = \frac{E_{sam} - N \times E_{mol}}{N}$$

where E_{bind} is the binding energy, E_{sam} is the potential energy of free-standing self-assembly, E_{mol} represents the potential energy of individual molecule when adsorbed on the substrate and N is the total number of the molecules in the self-assembly (note that by freezing the surface, its energy is 0 and can be ignored for the calculation of E_{bind}). The resulting binding energy for TTF-$(SC_{18})_4$ in the monolayer and in the second layer of the bilayer assembly was found to be −8.6 kcal/mol and −53.8 kcal/mol, respectively. The much higher stability for the second layer of the bilayer comes from the more compact packing of the molecules as well as the fully interdigitated organization of the alkyl chains. Such higher binding energy indicates that the molecules have a strong preference to form the bilayer structure, which can therefore persist even at low-concentration regime.

4. CONCLUSIONS

This combined experimental (STM) and modeling approach (molecular mechanics, molecular dynamics, DFT) brings insight into the self-assembly of a TTF derivative at the solution/graphite interface. Two assembly structures are found. A bilayer network, governed by $\pi-\pi$ stacking, is the predominant structure. Additionally, a more loosely packed monolayer network, sustained by the coadsorption of solvent molecules, is also observed. The latter is counterintuitively observed only at higher concentrations, which may find its origin in the presence of TTF particles in solution, as revealed

https://doi.org/10.1021/acs.jpcc.3c04913
J. Phys. Chem. C 2023, 127, 23023−23033

by UV/vis spectroscopy. We also found that the conformation of the TTF core, which can be linked to the experimental contrast seen in the two networks, is strongly affected by the length and the organization of the alkyl chains. This work is yet another testimony highlighting the often-complex nature of self-assembly at the liquid−solid interface, and the value of a combined experimental and theoretical approach to unveil factors impacting the self-assembly.

■ ASSOCIATED CONTENT

Supporting Information

The Supporting Information is available free of charge at https://pubs.acs.org/doi/10.1021/acs.jpcc.3c04913.

Experimental materials and methods, details of the molecular mechanics and molecular dynamics simulations, and additional and supporting STM data as well as supporting data from the simulations (PDF)

■ AUTHOR INFORMATION

Corresponding Authors

Kunal S. Mali − *Division of Molecular Imaging and Photonics, Department of Chemistry, KU Leuven, 3001 Leuven, Belgium;* orcid.org/0000-0002-9938-6446; Email: kunal.mali@kuleuven.be

Roberto Lazzaroni − *Laboratory for Chemistry of Novel Materials, Materials Research Institute, University of Mons, 7000 Mons, Belgium;* orcid.org/0000-0002-6334-4068; Email: roberto.lazzaroni@umons.ac.be

Steven De Feyter − *Division of Molecular Imaging and Photonics, Department of Chemistry, KU Leuven, 3001 Leuven, Belgium;* orcid.org/0000-0002-0909-9292; Email: steven.defeyter@kuleuven.be

Authors

Catarina L. Delfino − *Division of Molecular Imaging and Photonics, Department of Chemistry, KU Leuven, 3001 Leuven, Belgium*

Yansong Hao − *Electron Microscopy for Materials Science (EMAT) and NANOlab Center of Excellence, University of Antwerp, 2610 Antwerp, Belgium; Laboratory for Chemistry of Novel Materials, Materials Research Institute, University of Mons, 7000 Mons, Belgium;* orcid.org/0000-0001-8997-0430

Cristina Martin − *Department of Physical Chemistry, Faculty of Pharmacy, University of Castilla-La Mancha, 02071 Albacete, Spain*

Andrea Minoia − *Laboratory for Chemistry of Novel Materials, Materials Research Institute, University of Mons, 7000 Mons, Belgium*

Elumalai Gopi − *Laboratory of Polymer Chemistry, Faculty of Science, Université Libre de Bruxelles (ULB), 1050 Brussels, Belgium; International Solvay Institutes of Physics and Chemistry, ULB, 1050 Brussels, Belgium*

Mark Van der Auweraer − *Division of Molecular Imaging and Photonics, Department of Chemistry, KU Leuven, 3001 Leuven, Belgium*

Yves Henri Geerts − *Laboratory of Polymer Chemistry, Faculty of Science, Université Libre de Bruxelles (ULB), 1050 Brussels, Belgium; International Solvay Institutes of Physics and Chemistry, ULB, 1050 Brussels, Belgium;* orcid.org/0000-0002-2660-5767

Sandra Van Aert − *Electron Microscopy for Materials Science (EMAT) and NANOlab Center of Excellence, University of Antwerp, 2610 Antwerp, Belgium*

Complete contact information is available at: https://pubs.acs.org/10.1021/acs.jpcc.3c04913

Author Contributions

#Catarina L. Delfino and Yansong Hao made equal contributions.

Notes

The authors declare no competing financial interest.

■ ACKNOWLEDGMENTS

Financial support from the Research Foundation-Flanders (FWO G081518N, G0A3220N) and KU Leuven-Internal Funds (C14/19/079) is acknowledged. This work was in part supported by FWO and F. R. S.-FNRS under the Excellence of Science EOS program (project 30489208 and 40007495). C.M. acknowledges the financial support of Grants PID2021-128761OA-C22 and CNS2022-136052 funded by MCIN/AEI/10.13039/501100011033 by the "European Union" and SBPLY/21/180501/000127 funded by JCCM and by the EU through "Fondo Europeo de Desarollo Regional" (FEDER). Research in Mons is also supported by the Belgian National Fund for Scientific Research (FRS-FNRS) within the Consortium des Équipements de Calcul Intensif-CÉCI, under Grant 2.5020.11 and by the Walloon Region (ZENOBE Tier-1 supercomputer, under Grant 1117545).

■ REFERENCES

(1) Mali, K. S.; Pearce, N.; De Feyter, S.; Champness, N. R. Frontiers of Supramolecular Chemistry at Solid Surfaces. *Chem. Soc. Rev.* **2017**, *46*, 2520−2542.

(2) Goronzy, D. P.; Ebrahimi, M.; Rosei, F.; Arramel; Fang, Y.; De Feyter, S.; Tait, S. L.; Wang, C.; Beton, P. H.; Wee, A. T. S.; et al. Supramolecular Assemblies on Surfaces: Nanopatterning, Functionality, and Reactivity. *ACS Nano* **2018**, *12*, 7445−7481.

(3) Ciesielski, A.; Palma, C.-A.; Bonini, M.; Samorì, P. Towards Supramolecular Engineering of Functional Nanomaterials: Pre-Programming Multi-Component 2d Self-Assembly at Solid-Liquid Interfaces. *Adv. Mater.* **2010**, *22*, 3506−3520.

(4) Xing, L.; Peng, Z.; Li, W.; Wu, K. On Controllability and Applicability of Surface Molecular Self-Assemblies. *Acc. Chem. Res.* **2019**, *52*, 1048−1058.

(5) Xie, R.; Hu, Y.; Lee, S.-L. A Paradigm Shift from 2d to 3d: Surface Supramolecular Assemblies and Their Electronic Properties Explored by Scanning Tunneling Microscopy and Spectroscopy. *Small* **2023**, *19*, 2300413.

(6) Korolkov, V. V.; Svatek, S. A.; Summerfield, A.; Kerfoot, J.; Yang, L.; Taniguchi, T.; Watanabe, K.; Champness, N. R.; Besley, N. A.; Beton, P. H. Van Der Waals-Induced Chromatic Shifts in Hydrogen-Bonded Two-Dimensional Porphyrin Arrays on Boron Nitride. *ACS Nano* **2015**, *9*, 10347−10355.

(7) Puigmartí-Luis, J.; Minoia, A.; Uji-i, H.; Rovira, C.; Cornil, J.; De Feyter, S.; Lazzaroni, R.; Amabilino, D. B. Noncovalent Control for Bottom-up Assembly of Functional Supramolecular Wires. *J. Am. Chem. Soc.* **2006**, *128*, 12602−12603.

(8) Zhou, H.; Dang, H.; Yi, J.-H.; Nanci, A.; Rochefort, A.; Wuest, J. D. Frustrated 2D Molecular Crystallization. *J. Am. Chem. Soc.* **2007**, *129*, 13774−13775.

(9) Lee, S.-L.; Lin, H.-A.; Lin, Y.-H.; Chen, H.-H.; Liao, C.-T.; Lin, T.-L.; Chu, Y.-C.; Hsu, H.-F.; Chen, C.-h.; Lee, J.-J.; et al. Gearing of Molecular Swirls: Columnar Packing of Nematogenic Hexakis(4-Alkoxyphenylethynyl)Benzene Derivatives. *Chem. Eur. J.* **2011**, *17*, 792−799.

(10) Lei, S.; Tahara, K.; Feng, X.; Furukawa, S.; De Schryver, F. C.; Müllen, K.; Tobe, Y.; De Feyter, S. Molecular Clusters in Two-Dimensional Surface-Confined Nanoporous Molecular Networks: Structure, Rigidity, and Dynamics. *J. Am. Chem. Soc.* **2008**, *130*, 7119−7129.
(11) Afsharimani, N.; Minoia, A.; Volcke, C.; Surin, M.; Lazzaroni, R.; Balandier, J.-Y.; Niebel, C.; Geerts, Y. H.; Nysten, B. Self-Assembly of Alkyl-Substituted Oligothiophenes on Mos2: A Joint Experimental/Theoretical Study. *J. Phys. Chem. C* **2013**, *117*, 21743−21751.
(12) Klymchenko, A. S.; Furukawa, S.; Auweraer, M. V. d.; Müllen, K.; De Feyter, S. Directing the Assembly of Charged Organic Molecules by a Hydrophilic-Hydrophobic Nanostructured Monolayer at Electrified Interfaces. *Nano Lett.* **2008**, *8*, 1163−1168.
(13) Mali, K. S.; Wu, D.; Feng, X.; Müllen, K.; Van der Auweraer, M.; De Feyter, S. Scanning Tunneling Microscopy-Induced Reversible Phase Transformation in the Two-Dimensional Crystal of a Positively Charged Discotic Polycyclic Aromatic Hydrocarbon. *J. Am. Chem. Soc.* **2011**, *133*, 5686−5688.
(14) Lei, S.-B.; Deng, K.; Yang, Y.-L.; Zeng, Q.-D.; Wang, C.; Jiang, J.-Z. Electric Driven Molecular Switching of Asymmetric Tris-(Phthalocyaninato) Lutetium Triple-Decker Complex at the Liquid/Solid Interface. *Nano Lett.* **2008**, *8*, 1836−1843.
(15) Tong, W.; Wei, Y.; Armbrust, K. W.; Zimmt, M. B. Dipolar Side Chain Control of Monolayer Morphology: Symmetrically Substituted 1,5-(Mono- and Diether) Anthracenes at the Solution-HOPG Interface. *Langmuir* **2009**, *25*, 2913−2923.
(16) Tahara, K.; Lei, S.; Mamdouh, W.; Yamaguchi, Y.; Ichikawa, T.; Uji-i, H.; Sonoda, M.; Hirose, K.; De Schryver, F. C.; De Feyter, S.; et al. Site-Selective Guest Inclusion in Molecular Networks of Butadiyne-Bridged Pyridino and Benzeno Square Macrocycles on a Surface. *J. Am. Chem. Soc.* **2008**, *130*, 6666−6667.
(17) Piot, L.; Marie, C.; Feng, X.; Müllen, K.; Fichou, D. Hierarchical Self-Assembly of Edge-on Nanocolumnar Superstructures of Large Disc-Like Molecules. *Adv. Mater.* **2008**, *20*, 3854−3858.
(18) Cristadoro, A.; Lieser, G.; Räder, H. J.; Müllen, K. Field-Force Alignment of Disc-Type Π Systems. *ChemPhysChem* **2007**, *8*, 586−591.
(19) Jung, T. A.; Schlittler, R. R.; Gimzewski, J. K. Conformational Identification of Individual Adsorbed Molecules with the Stm. *Nature* **1997**, *386*, 696−698.
(20) Zhang, R.; Yan, Q.; Shen, Y.; Gan, L.; Zeng, Q.-d.; Zhao, D.; Wang, C. Conformational Polymorphism of Multimeric Perylene Derivatives Observed by Using Scanning Tunneling Microscopy. *CrysteEngComm* **2011**, *13*, 5566−5570.
(21) Samorí, P.; Fechtenkötter, A.; Jäckel, F.; Böhme, T.; Müllen, K.; Rabe, J. P. Supramolecular Staircase Via Self-Assembly of Disklike Molecules at the Solid-Liquid Interface. *J. Am. Chem. Soc.* **2001**, *123*, 11462−11467.
(22) Steeno, R.; Minoia, A.; Lazzaroni, R.; Mali, K. S.; De Feyter, S. Host-Guest Chemistry under Confinement: Peeking at Early Self-Assembly Events. *Chem. Commun.* **2022**, *58*, 3138−3141.
(23) Bragança, A. M.; Minoia, A.; Steeno, R.; Seibel, J.; Hirsch, B. E.; Verstraete, L.; Ivasenko, O.; Müllen, K.; Mali, K. S.; Lazzaroni, R.; et al. Detection and Stabilization of a Previously Unknown Two-Dimensional (Pseudo)Polymorph Using Lateral Nanoconfinement. *J. Am. Chem. Soc.* **2021**, *143*, 11080−11087.
(24) Resel, R.; Koch, N.; Meghdadi, F.; Leising, G.; Athouel, L.; Froyer, G.; Hofer, F. A Polymorph Crystal Structure of Hexaphenyl Observed in Thin Films. *Cryst. Res. Technol.* **2001**, *36*, 47−54.
(25) Mänz, A.; Breuer, T.; Witte, G. Epitaxial Tetrathiafulvalene-Tetracyanoquinodimethane Thin Films on Kcl(100): New Preparation Methods and Observation of Interface-Mediated Thin Film Polymorph. *Crys. Growth Des.* **2015**, *15*, 395−403.
(26) Yang, J.; Erriah, B.; Hu, C. T.; Reiter, E.; Zhu, X.; López-Mejías, V.; Carmona-Sepúlveda, I. P.; Ward, M. D.; Kahr, B. A Deltamethrin Crystal Polymorph for More Effective Malaria Control. *Proc. Natl. Acad. Sci. U.S.A.* **2020**, *117*, 26633−26638.
(27) Dimitrakopoulos, C. D.; Brown, A. R.; Pomp, A. Molecular Beam Deposited Thin Films of Pentacene for Organic Field Effect Transistor Applications. *J. Appl. Phys.* **1996**, *80*, 2501−2508.
(28) Bouchoms, I. P. M.; Schoonveld, W. A.; Vrijmoeth, J.; Klapwijk, T. M. Morphology Identification of the Thin Film Phases of Vacuum Evaporated Pentacene on Sio2 Substrates. *Synth. Met.* **1999**, *104*, 175−178.
(29) Ehmann, H. M. A.; Werzer, O. Surface Mediated Structures: Stabilization of Metastable Polymorphs on the Example of Paracetamol. *Crys. Growth Des.* **2014**, *14*, 3680−3684.
(30) Simões, R. G.; Salzmann, I.; Resel, R.; Röthel, C.; Geerts, Y. H. Stabilization of the Metastable Form I of Piracetam by Crystallization on Silicon Oxide Surfaces. *Crys. Growth Des.* **2018**, *18*, 4123−4129.
(31) He, Y.; Kröger, J.; Wang, Y. Organic Multilayer Films Studied by Scanning Tunneling Microscopy. *ChemPhysChem* **2017**, *18*, 429−450.
(32) Ferreira, Q.; Delfino, C. L.; Morgado, J.; Alcácer, L. Bottom-up Self-Assembled Supramolecular Structures Built by Stm at the Solid/Liquid Interface. *Materials* **2019**, *12*, 382.
(33) Salzmann, I.; Nabok, D.; Oehzelt, M.; Duhm, S.; Moser, A.; Heimel, G.; Puschnig, P.; Ambrosch-Draxl, C.; Rabe, J. P.; Koch, N. Structure Solution of the 6,13-Pentacenequinone Surface-Induced Polymorph by Combining X-Ray Diffraction Reciprocal-Space Mapping and Theoretical Structure Modeling. *Crys. Growth Des.* **2011**, *11*, 600−606.
(34) Resel, R.; Pichler, A.; Resel, R.; Neuhold, A.; Dingemans, T.; Schwabegger, G.; Simbrunner, C.; Moret, M.; Salzmann, I. Crystal Structure Determination of Organic Thin-Films: The Example of 2,2′:6′,2″-Ternaphthalene. *Zeitschrift für Kristallographie - Crystalline Materials* **2014**, *229*, 385−393.
(35) Jones, A. O. F.; Röthel, C.; Lassnig, R.; Bedoya-Martínez, O. N.; Christian, P.; Salzmann, I.; Kunert, B.; Winkler, A.; Resel, R. Solution of an Elusive Pigment Crystal Structure from a Thin Film: A Combined X-Ray Diffraction and Computational Study. *CrysteEngComm* **2017**, *19*, 1902−1911.
(36) Hao, Y.; Velpula, G.; Kaltenegger, M.; Bodlos, W. R.; Vibert, F.; Mali, K. S.; De Feyter, S.; Resel, R.; Geerts, Y. H.; Van Aert, S.; et al. From 2d to 3d: Bridging Self-Assembled Monolayers to a Substrate-Induced Polymorph in a Molecular Semiconductor. *Chem. Mater.* **2022**, *34*, 2238−2248.
(37) Fu, C.; Lin, H.-p.; Macleod, J. M.; Krayev, A.; Rosei, F.; Perepichka, D. F. Unravelling the Self-Assembly of Hydrogen Bonded Ndi Semiconductors in 2d and 3d. *Chem. Mater.* **2016**, *28*, 951−961.
(38) Bendikov, M.; Wudl, F.; Perepichka, D. F. Tetrathiafulvalenes, Oligoacenenes, and Their Buckminsterfullerene Derivatives: The Brick and Mortar of Organic Electronics. *Chem. Rev.* **2004**, *104*, 4891−4946.
(39) Gorgues, A.; Hudhomme, P.; Sallé, M. Highly Functionalized Tetrathiafulvalenes: Riding Along the Synthetic Trail from Electrophilic Alkynes. *Chem. Rev.* **2004**, *104*, 5151−5184.
(40) Bryce, M. R. Recent Progress on Conducting Organic Charge-Transfer Salts. *Chem. Soc. Rev.* **1991**, *20*, 355−390.
(41) Souto, M.; Santiago-Portillo, A.; Palomino, M.; Vitórica-Yrezábal, I. J.; Vieira, B. J. C.; Waerenborgh, J. C.; Valencia, S.; Navalón, S.; Rey, F.; García, H.; et al. A Highly Stable and Hierarchical Tetrathiafulvalene-Based Metal-Organic Framework with Improved Performance as a Solid Catalyst. *Chem. Sci.* **2018**, *9*, 2413−2418.
(42) Zu, X.; Li, J.; Qian, Y.; Duan, W.; Zeng, Q. Progress in Self-Assembly of TTF Derivatives at Hopg Interface. *New J. Chem.* **2019**, *43*, 1654−1662.
(43) Soler, J. M; Artacho, E.; Gale, J. D; García, A.; Junquera, J.; Ordejón, P.; Sánchez-Portal, D. The Siesta Method for Ab Initio Order- N Materials Simulation. *J. Phys.: Condens. Matter* **2002**, *14*, 2745.
(44) Perdew, J. P.; Burke, K.; Ernzerhof, M. Generalized Gradient Approximation Made Simple. *Phys. Rev. Lett.* **1996**, *77*, 3865−3868.
(45) Troullier, N.; Martins, J. L. Efficient Pseudopotentials for Plane-Wave Calculations. *Phys. Rev. B* **1991**, *43*, 1993−2006.

(46) Monkhorst, H. J.; Pack, J. D. Special Points for Brillouin-Zone Integrations. *Phys. Rev. B* **1976**, *13*, 5188−5192.
(47) Grimme, S. Semiempirical GGA-Type Density Functional Constructed with a Long-Range Dispersion Correction. *J. Comput. Chem.* **2006**, *27*, 1787−1799.
(48) Horcas, I.; Fernández, R.; Gómez-Rodríguez, J. M.; Colchero, J.; Gómez-Herrero, J.; Baro, A. M. Wsxm: A Software for Scanning Probe Microscopy and a Tool for Nanotechnology. *Rev. Sci. Instrum.* **2007**, *78*, 013705.
(49) *Biovia Materials Studio*; Dassault Systèmes: San Diego, CA, 2018. (accessed August 2023).
(50) Rappe, A. K.; Casewit, C. J.; Colwell, K. S.; Goddard, W. A., III; Skiff, W. M. UFF, a Full Periodic Table Force Field for Molecular Mechanics and Molecular Dynamics Simulations. *J. Am. Chem. Soc.* **1992**, *114*, 10024−10035.
(51) Casewit, C. J.; Colwell, K. S.; Rappe, A. K. Application of a Universal Force Field to Organic Molecules. *J. Am. Chem. Soc.* **1992**, *114*, 10035−10046.
(52) Abdel-Mottaleb, M. M. S.; Gomar-Nadal, E.; Surin, M.; Uji-i, H.; Mamdouh, W.; Veciana, J.; Lemaur, V.; Rovira, C.; Cornil, J.; Lazzaroni, R.; et al. Self-Assembly of Tetrathiafulvalene Derivatives at a Liquid/Solid Interface-Compositional and Constitutional Influence on Supramolecular Ordering. *J. Mater. Chem.* **2005**, *15*, 4601−4615.
(53) *Gaussian 16 Rev. B.01*; Gaussian: Wallingford, CT, 2016. (accessed.
(54) Becke, A. D. Density-Functional Exchange-Energy Approximation with Correct Asymptotic Behavior. *Phys. Rev. A* **1988**, *38*, 3098−3100.
(55) Lee, C.; Yang, W.; Parr, R. G. Development of the Colle-Salvetti Correlation-Energy Formula into a Functional of the Electron Density. *Phys. Rev. B* **1988**, *37*, 785−789.
(56) Becke, A. D. Density-Functional Thermochemistry. iii. The Role of Exact Exchange. *J. Chem. Phys.* **1993**, *98*, 5648−5652.
(57) Stephens, P. J.; Devlin, F. J.; Chabalowski, C. F.; Frisch, M. J. Ab Initio Calculation of Vibrational Absorption and Circular Dichroism Spectra Using Density Functional Force Fields. *J. Phys. Chem.* **1994**, *98*, 11623−11627.
(58) Vosko, S. H.; Wilk, L.; Nusair, M. Accurate Spin-Dependent Electron Liquid Correlation Energies for Local Spin Density Calculations: A Critical Analysis. *Can. J. Phys.* **1980**, *58*, 1200−1211.
(59) Samoletov, A. A.; Dettmann, C. P.; Chaplain, M. A. J. Thermostats for "Slow" Configurational Modes. *J. Stat. Phys.* **2007**, *128*, 1321−1336.
(60) Ghosh, S.; Chopra, P.; Wategaonkar, S. C-H···S Interaction Exhibits All the Characteristics of Conventional Hydrogen Bonds. *Phys. Chem. Chem. Phys.* **2020**, *22*, 17482−17493.
(61) Gao, F.; Zhu, F.-F.; Wang, X.-Y.; Xu, Y.; Wang, X.-P.; Zuo, J.-L. Stabilizing Radical Cation and Dication of a Tetrathiafulvalene Derivative by a Weakly Coordinating Anion. *Inorg. Chem.* **2014**, *53*, 5321−5327.
(62) Wang, L.; Zhang, J.-P.; Zhang, B. 4,4',5,5′-Tetrakis-(Methylsulfanyl)Tetrathiafulvalene. *Acta Crystallogr. E: Crystallogr.* **2005**, *61*, o65−o66.
(63) Thulstrup, P. W.; Hoffmann, S. V.; Jones, N. C.; Spanget-Larsen, J. Electronic Transitions of Tetrathiafulvalene Oriented in Polyethylene Film. Near and Vacuum UV Synchrotron Radiation Polarization Spectroscopy. *Chem. Phys. Imp.* **2021**, *2*, 100009.
(64) Velpula, G.; Martin, C.; Daelemans, B.; Hennrich, G.; Van der Auweraer, M.; Mali, K. S.; De Feyter, S. Concentration-in-Control" Self-Assembly Concept at the Liquid-Solid Interface Challenged. *Chem. Sci.* **2021**, *12*, 13167−13176.
(65) Wudl, F.; Kruger, A. A.; Kaplan, M. L.; Hutton, R. S. Unsymmetrical Dimethyltetrathiafulvalene. *J. Org. Chem.* **1977**, *42*, 768−770.
(66) Coffen, D. L.; Chambers, J. Q.; Williams, D. R.; Garrett, P. E.; Canfield, N. D. Tetrathioethylenes. *J. Am. Chem. Soc.* **1971**, *93*, 2258−2268.
(67) Nair, M. N.; Mattioli, C.; Cranney, M.; Malval, J.-P.; Vonau, F.; Aubel, D.; Bubendorff, J.-L.; Gourdon, A.; Simon, L. Stm Studies of Self-Assembled Tetrathiafulvalene (TTF) Derivatives on Graphene: Influence of the Mode of Deposition. *J. Phys. Chem. C* **2015**, *119*, 9334−9341.
(68) Sun, X.; Lai, G.; Li, Z.; Ma, Y.; Yuan, X.; Shen, Y.; Wang, C. Urethane Tetrathiafulvalene Derivatives: Synthesis, Self-Assembly and Electrochemical Properties. *Beilstein J. Org. Chem.* **2015**, *11*, 2343−2349.
(69) Pop, F.; Laroussi, S.; Cauchy, T.; Gomez-Garcia, C. J.; Wallis, J. D.; Avarvari, N. Tetramethyl-Bis(Ethylenedithio)-Tetrathiafulvalene (Tm-Bedt-Ttf) Revisited: Crystal Structures, Chiroptical Properties, Theoretical Calculations, and a Complete Series of Conducting Radical Cation Salts. *Chirality* **2013**, *25*, 466−474.
(70) Cea, P.; Morand, J. P.; Urieta, J. S.; Lopez, M. C.; Royo, F. M. Langmuir-Blodgett Mixed Films of a Tetrathiafulvalene Derivative and Behenic Acid: A Spectral Study. *Langmuir* **1996**, *12*, 1541−1544.
(71) Kilitziraki, M.; Moore, A. J.; Petty, M. C.; Bryce, M. R. Evaporated Thin Films of Tetrathiafulvalene Derivatives and Their Charge-Transfer Complexes. *Thin Solid Films* **1998**, *335*, 209−213.
(72) Kotarba, S.; Jung, J.; Kowalska, A.; Marszalek, T.; Kozanecki, M.; Miskiewicz, P.; Mas-Torrent, M.; Rovira, C.; Veciana, J.; Puigmarti-Luis, J.; et al. Anisotropy in Structural and Physical Properties in Tetrathiafulvalene Derivatives-Based Zone-Cast Layers as Seen by Raman Spectroscopy, Uv-Visible Spectroscopy, and Field Effect Measurements. *J. Appl. Phys.* **2010**, *108*, 014504.
(73) Cea, P.; Dominguez, M.; Urieta, J. S.; Lopez, M. C.; Royo, F. M. Tetrakis(Octadecylthio)Tetrathiafulvalene: Influence of Long Alkyl Chains on the Architecture and Electrochemical Properties of Lb Films. *J. Colloid Interface Sci.* **2001**, *237*, 112−119.
(74) Pérez-Rentero, S.; Eritja, R.; Häring, M.; Saldías, C.; Díaz, D. D. Synthesis, Characterization, and Self-Assembly of a Tetrathiafulvalene (TTF)-Triglycyl Derivative. *Appl. Sci.* **2018**, *8*, 671.
(75) Pou-AméRigo, R.; Viruela, P. M.; Viruela, R.; Rubio, M.; Ortı, E. Electronic Spectra of Tetrathiafulvalene and Its Radical Cation: Analysis of the Performance of the Time-Dependent Dft Approach. *Chem. Phys. Lett.* **2002**, *352*, 491−498.
(76) Scheblykin, I. G.; Varnavsky, O. P.; Verbouwe, W.; De Backer, S.; Van der Auweraer, M.; Vitukhnovsky, A. G. Relaxation Dynamics of Excitons in J-Aggregates Revealing a Two-Component Davydov Splitting. *Chem. Phys. Lett.* **1998**, *282*, 250−256.
(77) Van der Auweraer, M.; Scheblykin, I. One-Dimensional J-Aggregates: Dependence of the Properties of the Exciton Band on the Model of the Intermolecular Coupling. *Chem. Phys.* **2002**, *275*, 285−306.
(78) Van Der Auweraer, M.; Biesmans, G.; De Schryver, F. C. On the Photophysical Properties of Aggregates of 3-(2-Phenyl)-Indolocarbocyanines. *Chem. Phys.* **1988**, *119*, 355−375.
(79) Biesmans, G.; Van der Auweraer, M.; De Schryver, F. C. Influence of Deposition Circumstances on the Spectroscopic Properties of Mixed Monolayers of Dioctadecyloxacarbocyanine and Arachidic Acid. *Langmuir* **1990**, *6*, 277−285.
(80) Zimmer, K.; Gödicke, B.; Hoppmeier, M.; Meyer, H.; Schweig, A. Fluorescence Spectroscopic Studies on the Radical Cations of Tetrathiafulvalenes. *Chem. Phys.* **1999**, *248*, 263−271.
(81) Kilitziraki, M.; Pearson, C.; Dhindsa, A. S.; Bryce, M. R.; Petty, M. C. A Comparison of Tetrathiafulvalene Thin Films Prepared by Thermal Evaporation and the Langmuir-Blodgett Technique. *Thin Solid Films* **1996**, *284−285*, 516−519.
(82) Schröder, H. V.; Schalley, C. A. Tetrathiafulvalene - a Redox-Switchable Building Block to Control Motion in Mechanically Interlocked Molecules. *Beilstein J. Org. Chem.* **2018**, *14*, 2163−2185.
(83) Kauscher, U.; Bartels, K.; Schrader, I.; Azov, V. A.; Ravoo, B. J. Metastable Oxidation States of Tetrathiafulvalenes on the Surface of Liposomes. *J. Mater. Chem. B* **2015**, *3*, 475−480.
(84) Zeng, X.; Hu, Y.; Xie, R.; Khan, S. B.; Lee, S.-L. Monolayer and Bilayer Formation of Molecular 2D Networks Assembled at the Liquid/Solid Interfaces by Solution-Based Drop-Cast Method. *Molecules* **2021**, *26*, 7707.

https://doi.org/10.1021/acs.jpcc.3c04913
J. Phys. Chem. C 2023, 127, 23023−23033